The Astrophysical Journal, 972:62 (9pp), 2024 September 1 https://doi.org/10.3847/1538-4357/ad6308

5–25 μm Galaxy Number Counts from Deep JWST Data

Meredith A. Stone[1], Stacey Alberts[1], George H. Rieke[1], Andrew J. Bunker[2], Jianwei Lyu (吕建伟)[1], Pablo G. Pérez-González[3], Irene Shivaei[3], and Yongda Zhu[1]
[1] Steward Observatory, University of Arizona, 933 North Cherry Avenue, Tucson, AZ 85719, USA; meredithstone@arizona.edu
[2] Department of Physics, University of Oxford, Denys Wilkinson Building, Keble Road, Oxford OX1 3RH, UK
[3] Centro de Astrobiología (CAB), CSIC-INTA, Ctra. de Ajalvir km 4, Torrejón de Ardoz, E-28850, Madrid, Spain
Received 2024 May 10; revised 2024 July 9; accepted 2024 July 10; published 2024 August 26

Abstract

Galaxy number counts probe the evolution of galaxies over cosmic time and serve as a valuable comparison point to theoretical models of galaxy formation. We present new galaxy number counts in eight photometric bands between 5 and 25 μm from the Systematic Mid-infrared Instrument Legacy Extragalactic Survey and the JWST Advanced Deep Extragalactic Survey deep MIRI parallel, extending to unprecedented depth. By combining our new MIRI counts with existing data from Spitzer and AKARI, we achieve counts across 3–5 orders of magnitude in flux in all MIRI bands. Our counts diverge from predictions from recent semianalytical models of galaxy formation, likely due to their treatment of mid-IR aromatic features. Finally, we integrate our combined JWST −Spitzer counts at 8 and 24 μm to measure the cosmic infrared background (CIB) light at these wavelengths; our measured CIB fluxes are consistent with those from previous mid-IR surveys but larger than predicted by models based on TeV blazar data.

Unified Astronomy Thesaurus concepts: Galaxy counts (588)

1. Introduction

The distribution of the number of sources detected in a given filter as a function of flux, known as source counts or number counts, probes galaxy evolution on the largest scales and provides a direct observational comparison to the results of cosmological simulations and semianalytical models of galaxy formation and evolution. Unlike luminosity or mass functions, which can only be constructed with robust redshift constraints (difficult to obtain for huge samples of galaxies, and with their own uncertainties), deriving number counts requires only sufficient depth, area, and robust measurements of source fluxes and is therefore subject to fewer sources of calibration bias when comparing to simulations.

Number counts at different wavelengths in the mid- and far-IR in particular have revealed a great deal about the evolution of galaxies across cosmic time. The Infrared Astronomical Satellite (IRAS) and Infrared Space Observatory (ISO) missions revealed that the distribution of mid- and far-IR number counts differs significantly from that of the optical and near-IR. While optical and near-IR counts display a "Euclidean" $dN/dS_\nu \propto S_\nu^{-2.5}$ slope down to faint fluxes, consistent with a nonevolving population of spiral and elliptical galaxies, counts at longer mid-IR wavelengths display a characteristic "bump" between fluxes of approximately 0.1 and 0.5 mJy before decaying at fainter fluxes, attributed to the rapidly evolving population of galaxies between the local Universe and $z \sim 2$ (see, e.g., Fazio et al. 2004). In the twenty-first century, mid- and far-IR number counts have been probed to fainter and fainter limits, and the contributions of different galaxy populations have been inferred, with observations from later generations of IR space telescopes, including Spitzer's IRAC (Fazio et al. 2004; Treister et al. 2006; Barmby et al. 2008; Ashby et al. 2009, 2015; Papovich et al. 2016; Lacy et al. 2021), IRS (Teplitz et al. 2011), and MIPS (Chary et al. 2004; Marleau et al. 2004; Papovich et al. 2004; Treister et al. 2006; Rocca-Volmerange et al. 2007; Béthermin et al. 2010; Clements et al. 2011) instruments and the AKARI mission (Pearson et al. 2010; Murata et al. 2014; Pearson et al. 2014; Davidge et al. 2017). Prior to 2022, these missions had pushed the 80% completeness limit to <100 μJy at 8 and 24 μm with Spitzer and somewhat higher in intermediate bands with AKARI.

With the launch of the James Webb Space Telescope (JWST), a wealth of new data will become available to probe number counts in the mid-IR with MIRI. As number counts from MIRI data are brand new and able to reach unprecedented depth and access sources fainter than ever observed, they provide critical constraints on the faint end of the distribution, a region that currently displays the most variation between different cosmological simulations and semianalytical models (see, e.g., Lacy et al. 2021). These theoretical models are not yet calibrated to match JWST observations, so JWST data provide an independent test of model validity.

Already, mid-IR number counts from MIRI have been published in the Stephan's Quintet ERS field (Ling et al. 2022) at 7.7, 10, and 15 μm and in a portion of the Cosmic Evolution Early Release Science (CEERS) field in the Extended Groth Strip (Kirkpatrick et al. 2023; Wu et al. 2023). These data extend down to 80% completeness limits ranging from 0.25 μJy at 7.7 μm to 13 μJy at 21 μm, in some filters extending more than two orders of magnitude deeper than the deepest pre-JWST data available. However, the small area of these surveys (of order 5 arcmin^2 in each field) limited their ability to connect to previous observations at the bright end and leaves them vulnerable to cosmic variance.

In this work, we present number counts derived from the Systematic Mid-infrared Instrument Extragalactic Survey (SMILES) in eight MIRI bands, supplemented by ultradeep MIRI parallel imaging at 7.7 μm observed as part of the JWST Advanced Deep Extragalactic Survey (JADES). The wider area

Table 1
80% Completeness Limits from SMILES and JADES in the MIRI Bands

Band	5σ Sensitivity (μJy)	80% Completeness Limit (μJy)	Area (arcmin^2)
(1)	(2)	(3)	(4)
F560W	0.20	0.20	34.8
F770W (JADES)	0.040	0.036	10.1
F770W	0.19	0.18	34.5
F1000W	0.38	0.36	34.3
F1280W	0.59	0.54	34.5
F1500W	0.68	0.63	34.5
F1800W	1.7	1.6	34.5
F2100W	2.8	2.2	34.5
F2550W	16	15	34.5

($\sim$34 arcmin^2) and complete mid-IR wavelength coverage of SMILES complement the incredibly deep data of the MIRI JADES parallel and previously existing Spitzer data, allowing us to probe IR emission across more than five orders of magnitude in flux and suppress cosmic variance by linking MIRI counts to those from wider Spitzer surveys. We introduce our observations in Section 2, outlining our data reduction and completeness correction processes and photometric accuracy tests performed. We describe the construction of the number counts and present our results in Section 3. In Section 4, we compare to a number of state-of-the-art theoretical models of galaxy formation and evolution. We also integrate our 7.7 and 21 μm counts to constrain the cosmic infrared background (CIB) light and compare the result with values deduced from TeV gamma-ray observations. We summarize in Section 5.

2. Data

The primary data sets for this work are MIRI imaging in the GOODS-S field from SMILES (PID 1207) at 5.6–25.5 μm (G. Rieke et al. 2024, in preparation, Alberts et al. 2024) and the ultradeep 7.7 μm parallel (S. Alberts et al. 2024, in preparation) from JADES (PID 1180; Eisenstein et al. 2023). SMILES is composed of 15 pointings ($\sim$34 arcmin^2) of moderate-depth exposures (10.7–36.4 minutes) in eight MIRI filters (excluding only F1130W), reaching 5σ point-source sensitivities of 0.20, 0.19, 0.38, 0.59, 0.68, 1.7, 2.8, and 16 μJy for F560W, F770W, F1000W, F1280W, F1500W, F1800W, F2100W, and F2550W, respectively, measured in apertures containing 65% of the encircled energy for each point-spread function (PSF) and then aperture corrected (see Section 2.2).

The JADES deep MIRI parallel is four pointings ($\sim$10 arcmin^2) totaling 43 hr of science time per pointing, reaching a 5σ point-source sensitivity of 21 nJy in F770W. The 5σ point-source sensitivities are shown in Table 1 and are generally 2–2.5$\times$ lower than predicted by ETC v3.0 up to F1800W.

The majority of the area of these two surveys falls on deep and medium JADES NIRCam imaging (Eisenstein et al. 2023), as well as the rich ancillary data in GOODS-S from facilities such as the Hubble Space Telescope (e.g., Giavalisco et al. 2004; Grogin et al. 2011).

2.1. Data Reduction

The data reduction for SMILES and the JADES MIRI parallel are broadly similar; a full description can be found in Alberts et al. (2024). Both data sets were reduced using v.1.12.5 of the JWST calibration pipeline (Bushouse et al. 2023) using JWST Calibration Reference System (CRDS) context jwst_1188.pmap.

We supplement the standard pipeline with custom, external routines to remove warm pixels missed by the pipeline, "super" background subtraction (Pérez-González et al. 2024), and apply astrometry corrections, matched to GAIA through the JADES NIRCam catalog (Rieke et al. 2023). The final astrometry is accurate to 0.″1−0.″2 (1σ, per axis) for F560W–F2100W and 0.″4 for F2550W, as imaging in this filter is relatively shallow compared to the rest of the survey, with fewer detections suitable for deriving an astrometric correction (Alberts et al. 2024).

2.2. Source Extraction and Photometry

Blind MIRI photometric catalogs are created with a modified version of the JADES photometric pipeline (Rieke et al. 2023; S. Tacchella et al. 2024, in preparation). Object detection is done using a stacked F560W and F770W signal-to-noise ratio (SNR) image for SMILES and F770W only for the JADES parallel; these detection images are then used to create a robust segmentation map through an iterative process that starts at a low threshold for detection and then performs deblending, cleaning to remove spurious noise spikes, and faint source detection.

Circular aperture photometry (in apertures of diameter 0.″5, 0.″6, 0.″7, and 1.″0) is then measured from the final, clean segmentation map using PHOTUTILS with the windowed centroiding algorithm from SExtractor. Kron photometry (2.5$\times$ scaled) is also measured using a stacked signal map to define source centroids. Kron apertures smaller than our smallest circular aperture ($d = 0.''5$) are replaced with that circular aperture photometry. SMILES photometry in filters longer than F770W is measured using the apertures defined by the stacked F560W+F770W detection image. We assess whether this approach misses long-wavelength-only detections and/or changes the derived long-wavelength flux densities; we find that these effects are small and that our photometric catalog is robust (Alberts et al. 2024).

Aperture corrections are applied to both the circular aperture and Kron aperture fluxes using custom PSFs. We derive the aperture corrections for the latter by measuring the fraction of the PSF flux that falls outside each Kron aperture, to account for the size and shape of the PSF. For F1000W–F2550W, PSFs are created using WebbPSF (Perrin et al. 2014). For F560W and F770W, the PSF modeling is complicated by the cross-like imaging artifact known as the "cruciform" (Gáspár et al. 2021), and so empirical PSFs are constructed using high dynamic range imaging of stars obtained during JWST commissioning (A. Gáspár, private communication). Finally, photometric uncertainties are obtained using randomly placed apertures across the mosaics, accounting for local exposure time and correlated pixel noise (e.g., Whitaker et al. 2011; Rieke et al. 2023).

The final SMILES photometric catalog has 3591 sources with SNR > 4 in either the F560W or F770W filter. The JADES MIRI parallel catalog has 2860 sources with SNR > 4 in F770W.

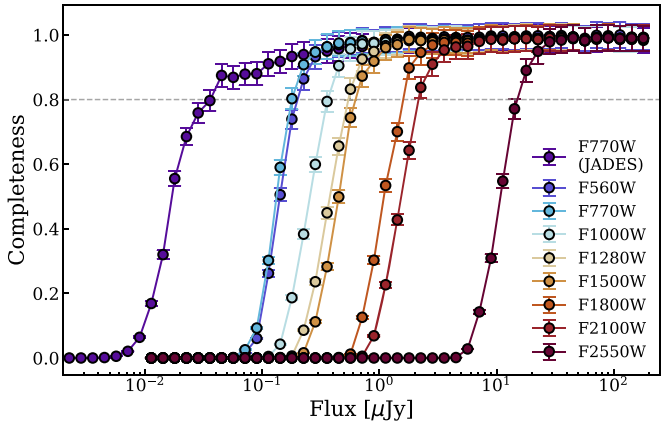

Figure 1. Completeness fraction as a function of flux for our MIRI data, including the JADES parallel F770W data (purple leftmost points) and the eight bands observed in SMILES. The 80% completeness threshold, which is the lower limit to which we report our number counts, is shown as a gray dashed line.

2.3. Completeness and Photometric Accuracy

We measure the completeness—the probability of measuring a source at a given flux density given the mosaic noise properties—in our images by inserting and measuring the recovery rate of artificial point sources constructed from our PSFs (Section 2.2). We derive the completeness using point sources because faint galaxies are predominantly intrinsically small and unresolved or marginally resolved by MIRI, while MIRI-resolved sources tend to be bright. Bright extended sources are in a flux regime where the completeness corrections are negligible (see Figure 1), and we do not expect faint, extended sources (for which our completeness will be overestimated) to be numerous enough to significantly affect our counts.

For SMILES, artificial sources are inserted in 43 flux bins with a width of 0.1 dex ranging from 0.01 to 200 μJy. Within each bin, the flux of each artificial source is chosen at random. For each filter and flux bin, we generate 10 mosaics with 150 artificial sources (<5% of the real source catalog) inserted into random positions (with masking of the map edges), totaling 1500 artificial sources per filter per flux bin, a number that ensures robust Gaussian statistics while limiting computational time requirements. Photometric catalogs are then created for each altered mosaic following the procedure outlined in Section 2.2. Artificial sources are considered recovered if they are found within 0.″2 of the inserted position and the measured flux density is detected at $>2\sigma$ and within 50% of the input flux. The latter accounts for flux boosting of faint sources from brighter neighbors under the approximation that galaxies are randomly distributed. As galaxies are in reality clustered, this is an underestimation, but we do not expect this to have a significant impact on our measured number counts given the small MIRI beam (Viero et al. 2013).

This procedure is repeated for the JADES MIRI parallel, with 53 flux bins ranging from 0.001 to 200 μJy with 0.1 dex bin width. Given the smaller area of the parallel, we inject 50 artificial sources at a time into 30 mosaics, again producing 1500 artificial sources per flux bin. The resulting completeness curves for both surveys are shown in Figure 1, and the 80% completeness level is reported in Table 1. A completeness of 80% in each band is reached at approximately the 5σ detection limit. This high completeness at faint fluxes is attributable to our careful background subtraction (Section 2.1). For the rest of this work, only sources above the 80% completeness limit will be considered.

2.4. Contamination by Spurious Sources

We expect some fraction of our detected sources to be spurious: not true astrophysical sources, but peaks in the noise. The contribution of these "false positives" to our number counts is certainly insignificant at the bright end of the distribution, but it may become important to the total counts at the faint end.

To quantify the fraction of spurious sources our counts contain, we perform a source extraction on negative images (see Papovich et al. 2004). By inverting the images, the flux of all real sources becomes negative, and the only positive sources remaining in the image are random Gaussian peaks from noise. As the noise is random, the number of sources in the negative image should also reflect the number of spurious sources that will be detected in the original images and removed from the counts.

We invert the mosaic in each filter and mask the noisy edges before performing source detection (using Photutils' find_peaks algorithm), extracting photometry with a 1.″2-diameter aperture. We find that the vast majority of spurious sources have integrated fluxes well below our completeness limits, with only a few noise peaks bright enough to contribute to the faint end of the counts. Normalizing by the areas of SMILES and JADES, we find that we expect $\sim$0.05–0.25 counts arcmin^{-2} from spurious sources at the 80% completeness limits of SMILES, and even fewer in the JADES parallel. Contributions from spurious sources at brighter fluxes are, as expected, completely negligible, and we therefore make no corrections accounting for their presence.

3. Results

3.1. Constructing Number Counts

Differential and cumulative number counts are derived from the photometric catalogs described in Section 2.2. Precise individual areas are measured for each mosaic by counting unmasked pixels (Table 1). The exposure times are largely uniform across the mosaics: 70%–80% of pixels have exposure times within 5% of the median.

We consider counts in each filter down to the 80% completeness limits, which are comparable to the 5σ point-source sensitivities (Table 1). The number counts discussed in the following sections and reported in Table 2 are completeness corrected, and the error bars reflect purely statistical error.

3.2. Number Counts at 7.7 μm

Our deepest data are at 7.7 μm. At low redshift, F770W traces the mid-IR polycyclic aromatic hydrocarbon (PAH) features and probes the rest-frame peak of stellar emission at higher redshift, $z\sim2$ to -5. At all redshifts, 7.7 μm—and other mid-IR—counts will additionally contain a population of dust-obscured active galactic nuclei (AGNs) and composite (star-forming + AGN) galaxies. When corrected for the contribution of AGNs, 7.7 μm counts can therefore test the distribution of stellar mass, particularly at high redshift, of galaxy formation models.

Table 2
Cumulative MIRI Number Counts from SMILES and JADES

Flux (μJy) (1)	F560W (2)	F770W (SMILES) (3)	F770W (JADES) (4)	F1000W (5)	F1280W (6)	F1500W (7)	F1800W (8)	F2100W (9)	F2550W (10)
3.98E−2	⋯	⋯	3218 ± 5	⋯	⋯	⋯	⋯	⋯	⋯
6.31E−2	⋯	⋯	167 ± 4	⋯	⋯	⋯	⋯	⋯	⋯
1.00E−1	⋯	⋯	130 ± 4	⋯	⋯	⋯	⋯	⋯	⋯
1.58E−1	⋯	⋯	104 ± 3	⋯	⋯	⋯	⋯	⋯	⋯
2.51E−1	71.3 ± 1.4	55.0 ± 1.3	81.8 ± 2.9	⋯	⋯	⋯	⋯	⋯	⋯
3.98E−1	52.2 ± 1.2	41.7 ± 1.1	64.5 ± 2.6	41.3 ± 1.1	⋯	⋯	⋯	⋯	⋯
6.31E−1	38.7 ± 1.1	32.6 ± 1.0	50.8 ± 2.3	31.1 ± 1.0	35.6 ± 1.0	39.3 ± 1.0	⋯	⋯	⋯
1.00E+0	30.0 ± 0.9	25.3 ± 0.9	41.2 ± 2.0	25.0 ± 0.9	27.1 ± 0.9	30.0 ± 0.9	⋯	⋯	⋯
1.58E+0	23.0 ± 0.8	20.6 ± 0.8	31.6 ± 1.8	20.0 ± 0.8	22.0 ± 0.8	24.1 ± 0.8	⋯	⋯	⋯
2.51E+0	18.0 ± 0.7	16.1 ± 0.7	23.6 ± 1.6	15.8 ± 0.7	18.0 ± 0.7	19.6 ± 0.8	22.7 ± 0.8	27.7 ± 0.9	⋯
3.98E+0	13.7 ± 0.6	11.7 ± 0.6	17.6 ± 1.3	12.1 ± 0.6	14.5 ± 0.6	15.6 ± 0.7	18.5 ± 0.7	21.0 ± 0.8	⋯
6.31E+0	9.73 ± 0.53	8.48 ± 0.50	12.5 ± 1.1	8.81 ± 0.51	11.2 ± 0.6	12.7 ± 0.6	15.0 ± 0.7	16.4 ± 0.7	⋯
1.00E+1	6.60 ± 0.44	5.41 ± 0.40	8.01 ± 0.90	5.96 ± 0.42	8.67 ± 0.50	9.96 ± 0.54	12.6 ± 0.6	13.5 ± 0.6	⋯
1.58E+1	4.37 ± 0.35	3.17 ± 0.30	4.62 ± 0.69	4.16 ± 0.35	6.17 ± 0.42	7.81 ± 0.48	9.58 ± 0.53	10.7 ± 0.6	13.5 ± 0.6
2.51E+1	2.46 ± 0.27	1.79 ± 0.23	2.06 ± 0.46	2.92 ± 0.29	4.79 ± 0.37	5.99 ± 0.42	7.26 ± 0.46	8.29 ± 0.49	9.13 ± 0.51
3.98E+1	1.27 ± 0.19	0.85 ± 0.16	1.13 ± 0.34	1.86 ± 0.23	3.58 ± 0.32	4.41 ± 0.36	5.58 ± 0.40	6.23 ± 0.43	6.50 ± 0.43
6.31E+1	0.46 ± 0.12	0.35 ± 0.10	0.31 ± 0.18	1.27 ± 0.19	2.53 ± 0.27	3.03 ± 0.30	4.03 ± 0.34	4.12 ± 0.35	4.41 ± 0.36
1.00E+2	0.12 ± 0.06	0.21 ± 0.08	0.10 ± 0.10	0.83 ± 0.16	1.73 ± 0.22	1.91 ± 0.24	2.58 ± 0.27	2.79 ± 0.28	2.70 ± 0.28
1.58E+2	0.06 ± 0.04	0.18 ± 0.07	⋯	0.53 ± 0.12	0.91 ± 0.16	0.94 ± 0.17	1.56 ± 0.21	1.47 ± 0.21	1.53 ± 0.21
2.51E+2	⋯	0.09 ± 0.05	⋯	0.24 ± 0.08	0.56 ± 0.13	0.53 ± 0.12	0.68 ± 0.14	0.79 ± 0.15	0.76 ± 0.15
3.98E+2	⋯	0.06 ± 0.04	⋯	0.21 ± 0.08	0.26 ± 0.09	0.21 ± 0.08	0.29 ± 0.09	0.35 ± 0.10	0.32 ± 0.10
6.31E+2	⋯	0.03 ± 0.03	⋯	0.12 ± 0.06	0.09 ± 0.05	0.09 ± 0.05	0.12 ± 0.06	0.09 ± 0.05	0.18 ± 0.07
1.00E+3	⋯	⋯	⋯	0.06 ± 0.04	0.06 ± 0.04	0.03 ± 0.03	0.03 ± 0.03	0.03 ± 0.03	0.06 ± 0.04

Note. All reported counts (2–10) are cumulative ($N > S_\nu$), with units arcmin^{-2}.

The similarity between the MIRI F770W and Spitzer/IRAC Channel 4 (8 μm) filters also allows us to connect our very deep counts with those from wide-field Spitzer surveys, probing both the bright and faint ends of the distribution. However, the two filters are not identical. While the MIRI F770W filter has slightly higher throughput, the IRAC-4 bandpass is wider on the red side, extending to $\sim$9.5 μm compared to F770W's $\sim$8.75 μm. The largest difference between an individual source's IRAC-4 and F770W fluxes will likely occur for sources at redshifts where a bright PAH feature is shifted out of the F770W bandpass but remains in the IRAC-4 bandpass, but this occurs in only two small redshift ranges ($z \sim 0.13$–0.27 and 0.41–0.52 for the 7.7 and 6.2 μm PAH features, respectively). Early JWST results comparing MIRI to IRAC counts indicate that the effect of this difference is very small (see, e.g., Wu et al. 2023; Yang et al. 2023) in the flux regime where MIRI and IRAC counts overlap.

We present our differential and cumulative 7.7 μm counts from SMILES and JADES in Figure 2, alongside bright-end IRAC-4 data from the Spitzer Deep Wide-Field Survey (SDWFS; Ashby et al. 2009). Together, these deep MIRI data and wide Spitzer data provide the deepest 8 μm counts ever observed, spanning more than five orders of magnitude in flux from $<$0.1 to more than 10^4 μJy.

The MIRI F770W counts in the SMILES and JADES fields are slightly offset from each other. We have verified that this offset is not due to any differences in the data reduction process. Instead, this is likely due to cosmic variance: the Hubble Ultra Deep Field (which forms the center of the SMILES footprint) is known to be slightly underdense, while a number of overdensities have already been cataloged in the small JADES parallel field (Alberts et al. 2023). The difference between the SMILES and JADES counts likely encodes the typical variation that will be observed between surveys (see also the variation in counts for fluxes probed by Spitzer; Béthermin et al. 2010).

The differential counts (right panel of Figure 2), which have been normalized to a Euclidean universe (multiplied by $S_\nu^{2.5}$), display the characteristic power-law decline toward faint fluxes observed by other telescopes and flatten at the bright end when we remove the contribution from Galactic stars from the model of Fazio et al. (2004).

For comparison, we also plot in Figure 2 the 8 μm number count predictions from a number of simulations and semi-analytical models of galaxy formation, namely the GALFORM semianalytical model and GRASIL radiative transfer code (F770W; Cowley et al. 2018), the SHARK semianalytical model (IRAC-4; Lagos et al. 2019), the SPRITZ simulations (F770W; Bisigello et al. 2021), and the IRAC-4 model of Rowan-Robinson (2009, 2024). We discuss these models in greater depth in Section 4.1.

3.3. Number Counts at 21 μm and 25 μm

We plot our SMILES cumulative and differential counts at both 21 and 25 μm in Figure 3, as the counts in both bands have very similar distributions. Our new JWST counts also align with counts from deep 24 μm Spitzer surveys (Papovich et al. 2004; Béthermin et al. 2010; plotted as gray squares and black plus signs, respectively), which we use to extend our distribution to the bright end. Together, these 21/24 μm counts extend over approximately four orders of magnitude, from less than 100 to more than 10^5 μJy, and probe deeper than any $\sim$24 μm counts previously published. Additionally, due to the

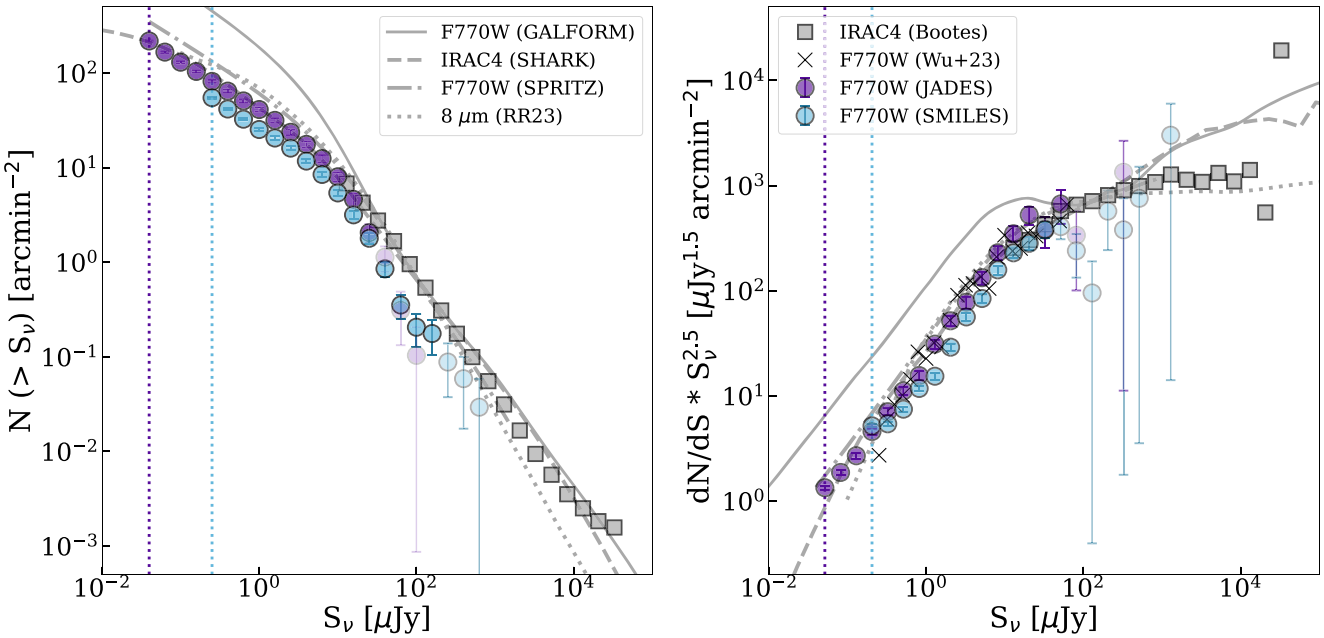

Figure 2. Cumulative (left) and Euclidean-normalized differential (right) number counts at 7.7 μm (MIRI) and 8 μm (IRAC). The deep MIRI F770W counts from JADES and SMILES are shown as purple and blue circles, respectively, and their 80% completeness limits are marked by colored dotted vertical lines. For visual clarity, points at the bright end with high scatter and large error bars are plotted with greater transparency. We also plot the differential F770W counts in two MIRI pointings in the CEERS field measured by Wu et al. (2023) (black crosses in the right panel), which agree very well with our data. We link our MIRI data to the bright end by including the IRAC 8 μm counts from SDWFS (Ashby et al. 2009) as gray squares: together these produce number counts spanning more than five orders of magnitude in flux. The Ashby et al. (2009) IRAC counts have had the contribution from Galactic stars subtracted according to predictions from Fazio et al. (2004). We also include for comparison predicted number counts at 8 μm from the GALFORM semianalytical model (Cowley et al. 2018; gray solid line), the SHARK semianalytical model (Lagos et al. 2019; gray dashed line), the SPRITZ simulations (Bisigello et al. 2021; gray dotted–dashed line), and the models of Rowan-Robinson (2009, 2024; gray dotted line). For ease of comparison, we normalize each model to the observed counts at 10^2 μJy.

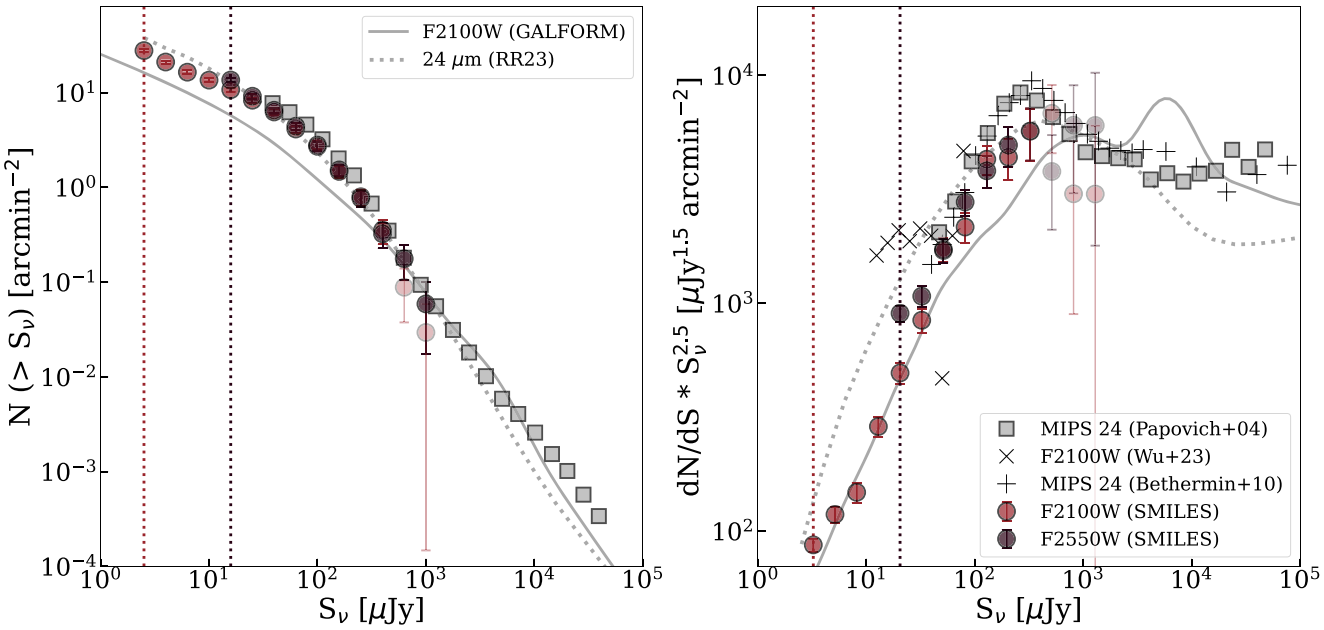

Figure 3. Number counts at 21 and 25 μm. We plot our cumulative (left) and Euclidean-normalized differential (right) MIRI SMILES F2100W and F2550W counts as colored circles (lighter red and darker brown, respectively). As in Figure 2, points at the bright end with high scatter and large error bars are plotted with greater transparency for visual clarity. Colored dotted vertical lines mark the 80% completeness limits of the SMILES 21 and 25 μm counts. We link to the bright end by including Spitzer/MIPS 24 μm counts from Papovich et al. (2004) (gray squares). These counts are not significantly contaminated by stars. For comparison, we also plot the differential F2100W counts in a portion of the CEERS field from Wu et al. (2023) at right as black crosses. We additionally include modeled number counts from the literature, from both the GALFORM semianalytical model (Cowley et al. 2018; gray solid line) and the models of Rowan-Robinson (2009, 2024) (gray dotted line). These models have been normalized to the counts at 10^3 μJy.

unprecedented spatial resolution of JWST, our MIRI ~24 μm counts are not confusion limited, unlike the Spitzer counts also shown in Figure 3.

The flux at ~25 μm probes the mid-IR warm dust continuum until $z \sim 1.5$, when the bright 7.7 μm PAH feature begins to shift into the band. We observe the characteristic bump at

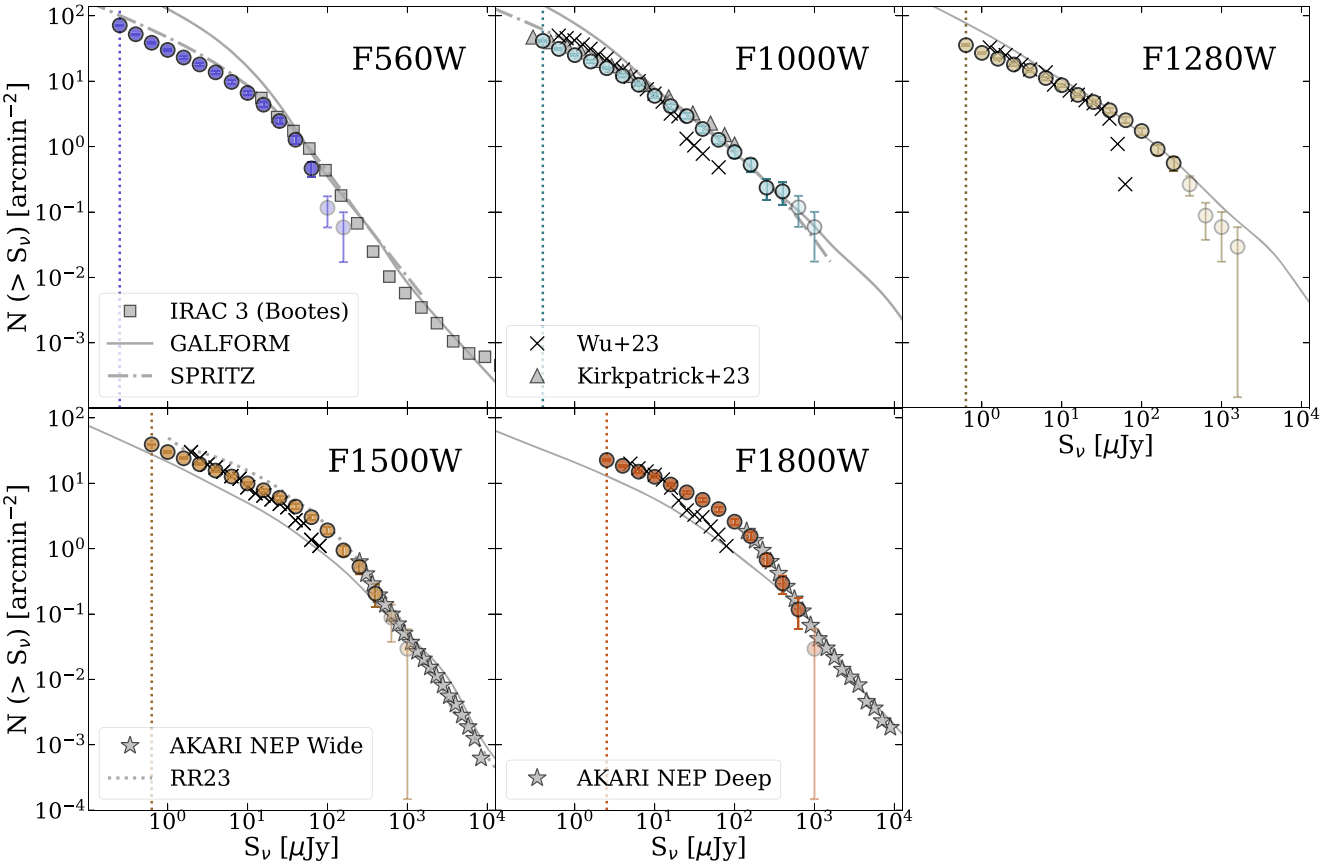

Figure 4. Cumulative number counts for the remaining MIRI bands. MIRI data from SMILES are plotted as colored circles, with colored dotted vertical lines marking the 80% completeness limit in each band. We also include model number counts in each band from the GALFORM semianalytical model (Cowley et al. 2018) as gray solid lines. All models have been normalized to the counts near the bright end (10^2 μJy at 5.6, 10, and 12.8 μm; 10^3 μJy at 15 and 18 μm). At 5.6 and 10 μm, we include the predictions of the SPRITZ simulations (Bisigello et al. 2021; gray dotted–dashed line). We extend the counts to slightly brighter fluxes by including data from SDWFS at 5.6 μm (Ashby et al. 2009, gray squares) and the AKARI NEP-Wide (Pearson et al. 2010) and NEP-Deep surveys (Pearson et al. 2014) at 15 and 18 μm, respectively (gray stars). We have corrected the IRAC 5.6 μm counts for the contribution from Galactic stars (Fazio et al. 2004). At 10, 12.8, 15, and 18 μm, we include MIRI number counts in two MIRI pointings of the CEERS field as black crosses (Wu et al. 2023). At 10 μm, counts from more extensive data in the CEERS survey are shown as gray triangles (Kirkpatrick et al. 2023).

$\sim$100 μJy in the Euclidean-normalized differential counts. Despite the minimal overlap of the MIRI F2100W and F2550W bands, the counts display very similar distributions down to the limit of the F2550W data.

The MIPS 24 μm filter is much broader than the MIRI filters, encompassing most of the wavelength range covered by the MIRI F2100W and F2550W filters. This discrepancy, however, does not appear to severely affect the magnitude or shape of the source counts' distribution, as the MIPS 24 μm data from Papovich et al. (2004) and Béthermin et al. (2010) display fair agreement, within the uncertainties and scatter, with the MIRI data. No correction has been applied to either the MIRI or MIPS counts to account for the very different bandpasses and bring the counts into alignment.

In addition to the Spitzer counts, we can compare our results to the counts obtained in two MIRI pointings of the CEERS survey by Wu et al. (2023). While the Wu et al. (2023) counts agree well with ours down to $\sim$100 μJy, their differential counts flatten at the faintest end of their data, between $\sim$10 and 100 μJy, rather than continuing to decrease as a power law like our SMILES counts or model predictions. This may be an artifact of those data's lack of background subtraction, as we observe a similar effect to a lesser extent in other bands longward of 10 μm (discussed below in Section 3.4).

In general, when normalized near 10^3 μJy, the models of Rowan-Robinson (2009, 2024) reasonably closely follow our observed counts down to the faint end and reproduce the shape of the differential number count distribution well (right panel of Figure 3). The GALFORM model, on the other hand, underpredicts the number of faint sources and does not exhibit the peak in the differential counts near 100 μJy seen in both JWST and Spitzer data. Further discussion of these comparisons can be found in Section 4.1.

3.4. Number Counts in Other Bands

We plot the cumulative number counts for all remaining MIRI bands (F560W, F1000W, F1280W, F1500W, and F1800W) in Figure 4. We include, when available, other data and models in the bands, including AKARI counts (Pearson et al. 2010, 2014), MIRI counts in the CEERS field (Kirkpatrick et al. 2023; Wu et al. 2023), and the GALFORM (Cowley et al. 2018), SPRITZ (Bisigello et al. 2021), and Rowan-Robinson (2009, 2024) models.

Counts from the AKARI North Ecliptic Pole (NEP) surveys at 15 and 18 μm (Pearson et al. 2010, 2014) extend our MIRI counts to the bright end and are in very good agreement with our counts where they overlap. As a result, the counts at 15 and 18 μm extend over nearly four orders of magnitude in flux. These AKARI counts have been corrected for the contributions

of stars, but not for the difference between the MIRI F1500W/F1800W and AKARI IRC $L15/L18$ bandpasses. The AKARI bandpasses are significantly broader than the corresponding MIRI bandpasses: for example, while the two filters have roughly the same central wavelength, $L15$'s half-power width (6.8 μm) is more than twice that of F1500W ($\sim$3.1 μm). Nonetheless, the excellent agreement of the AKARI counts with our MIRI data demonstrates that the different filter shapes do not strongly affect the counts.

At the fainter end, we can compare our counts to the slightly shallower counts measured in two of the MIRI pointings of the CEERS field by Wu et al. (2023). These counts, in F1000W, F1280W, F1500W, and F1800W, drop off quickly at $\sim$100 mJy, due to the smaller area of the survey, and do not go quite as deep. While they agree fairly well with our counts, some of the bands (particularly F1000W and F1800W) display steeper slopes between 1 and 100 μJy. This may be a background subtraction artifact, similar to that observed near the faint end at 21 μm (right panel of Figure 3). This hypothesis is reinforced by the 10 μm counts from Kirkpatrick et al. (2023): these data, also from the CEERS survey, agree well with our 10 μm counts.

3.5. Cosmic Variance

The error bars in Figures 2–4 reflect only statistical errors. Potentially larger errors occur because of cosmic variance: the differences in source characteristics among different fields on the sky (e.g., Trenti & Stiavelli 2008). Cosmic variance is reduced significantly as the number of distinct fields surveyed increases, and also with the area of the field(s) surveyed. In addition, the effects of cosmic variance are more pronounced for the brighter sources than the fainter ones (e.g., Driver & Robotham 2010; Robertson 2010; Moster et al. 2011).

By combining counts from the large-area, moderate-depth surveys of Spitzer and AKARI with the (to date) small areas surveyed to great depth by JWST, the cosmic variance effects at play can be understood and mitigated. We discuss cosmic variance for each wavelength in turn.

5.6 μm: The top left panel of Figure 4 compares our 5.6 μm counts with those in IRAC-3 reported in $\sim$8 deg^2 in the Bootes field by Ashby et al. (2009). The Ashby et al. (2009) counts demonstrate excellent agreement with those in the 0.38 deg^2 survey in the Extended Groth Strip surveyed to $\sim$5 times deeper reported by Barmby et al. (2008) and with counts from the IRAC Shallow Survey (Fazio et al. 2004). The large areas surveyed and the agreement of counts from two widely separated fields indicate that cosmic variance does not have a strong effect on these counts. Their close agreement with our JWST-based counts in the region of overlap indicates, despite the small area surveyed, that the latter counts are also representative without a large bias due to cosmic variance.

7.7 μm: Figure 2 compares our counts at 7.7 μm to those from Ashby et al. (2009) at 7.8 μm. As at 5.6 μm, the Ashby et al. (2009) 7.8 μm counts agree well with counts measured in other fields with Spitzer (Fazio et al. 2004; Barmby et al. 2008) and agree with our MIRI F770W counts where they overlap. We therefore do not expect cosmic variance to seriously bias our 7.7 μm counts.

15 and 18 μm: The counts in Figure 4 at 15 and 18 μm use results from the AKARI NEP surveys.[4] These observations were designed to reduce cosmic variance to the 5%−10% level (Pearson et al. 2010).[5] They cover areas of $\sim$0.4–0.6 deg^2 and 5.8 deg^2 to depths of 117 (150) and 250 (300) μJy, respectively, at 15 (18) μm (Pearson et al. 2010, 2014). The excellent agreement with the counts in the SMILES field in the region of overlap again implies that the entire range shown in Figure 4 is unlikely to be compromised by cosmic variance. On the other hand, MIRI counts from Wu et al. (2023) fall low at the bright end, suggestive of an influence of variance on those results, due possibly to the significantly smaller field available ($\sim$6 arcmin^2).

21–25 μm: Figure 3 compares JWST/MIRI counts at 21 and 25.5 μm with Spitzer/MIPS counts at 24 μm. The counts from Papovich et al. (2004) are from five widely separated fields with $\sim$0.61 deg^2 surveyed to a depth of $\sim$80 μJy and $>$10 deg^2 to a depth of at least 270 μJy. Béthermin et al. (2010) report surveys of $\sim$0.64 deg^2 to $\sim$80 μJy and 53 deg^2 to at least $\sim$400 μJy in seven additional fields. These surveys agree very well with each other and with our counts down to their limits of 80 μJy (see Figure 3). Again, this indicates that the full range of counts presented here is not strongly affected by cosmic variance.

4. Discussion

4.1. Models

Figures 2–4 show the predictions of number count models between 5 and 25 μm, many of which diverge from observed counts. Many models, even those published recently, use spectral energy distribution (SED) templates created before Spitzer IRS data were available and/or use relatively abstract templates that do not match the results with full Spitzer data (e.g., as in Rieke et al. 2008; Magdis et al. 2012; Schreiber et al. 2018; Bernhard et al. 2021). This could be important because the aromatic bands dominate the IR output of star-forming galaxies from 6 through 12 μm and fall within the wavelength range of JWST and Spitzer number counts for $z \sim$ 0–3. For example, Cowley et al. (2018) utilize a combination of models from GRASIL (Silva et al. 1998) and GALFORM (Granato et al. 2000). However, in these models the PAH bands are represented very schematically, and in the latter one the region between 15 and 40 μm is not represented accurately and the silicate absorption features at 10 and 18 μm are not included. The modeled number counts by Rowan-Robinson (2024) are based on mid-IR SEDs from Rowan-Robinson et al. (2004, 2005). These are constrained by Spitzer photometry, but the PAH bands are from ISO spectroscopy of a very small number of galaxies (Rowan-Robinson 2001) and again are quite schematic. This relatively limited sample of PAH spectra can cause problems: for an example, compare the proposed spectra in Figure 6 in Rowan-Robinson et al. (2005) for "Arp 220 starbursts" with the actual spectrum of Arp 220 from Spoon et al. (2004).

Two sets of models, SHARK (Lagos et al. 2019) and SPRITZ (Bisigello et al. 2021), do include accurate spectra of the PAH bands making use of Spitzer IRS spectra. The SHARK models are based on a semianalytic model (SAM) of galaxy formation and evolution. These models are compared with counts in the IRAC bands, and their good matching of the 7.7 μm counts presented here to very faint levels is very

[4] ISO counts at 15 μm were reported by Oliver et al. (1997) but have been supplanted by those from AKARI.

[5] The coverage of even larger (and more) fields in IRAC Band 4 and MIPS 24 μm reinforces our expectation that these surveys are not significantly affected by cosmic variance.

encouraging in terms of such models. Obviously, using this approach to model counts at the longer wavelengths is very desirable, continuing with accurate template SEDs. The SPRITZ models are empirically based on a global analysis of galaxy properties. They provide good fits out to 8 μm, including to our very deep 7.7 μm counts. At the longer wavelengths, their results are subject to substantial errors that undermine a quantitative assessment of their accuracy. For both sets of models, the agreement with our 7.7 μm counts demonstrates that representing the PAH bands accurately is critical to interpreting the number counts presented in this paper.

4.2. The Cosmic Infrared Background

The CIB is the fraction of the extragalactic background light (EBL) emitted in the IR and arises mainly from dust-obscured star formation (with contributions from dust-obscured AGNs) in galaxies across cosmic time (Hauser et al. 1998; Gispert et al. 2000; Lagache et al. 2005). With more sensitive telescopes, more and more of the CIB can be resolved into individual sources, e.g., the sources making up our galaxy number counts. Our discussion below follows on from the treatment in Driver et al. (2016).

To estimate the total 8 μm flux from sources detectable in our MIRI data, we combine and integrate 8 μm number counts from the SDWFS (Ashby et al. 2009) at the bright end, with stars removed, and our JADES MIRI parallel at the faint end. To combine the data sets, we exclude all JADES MIRI parallel counts at fluxes brighter than $S_\nu = 50$ μJy, because the counts in this flux regime are affected by cosmic variance owing to the small area of the survey. The wider-area SDWFS has data in this flux range, which will be less affected by cosmic variance. Correspondingly, we exclude all counts at fluxes fainter than $S_\nu = 30$ μJy from the SDWFS IRAC data: this flux corresponds to the 8 μm SDWFS 80% completeness limit. In the small remaining region of overlap, the MIRI and IRAC counts agree well (see Figure 2). We also do not include the two brightest SDWFS IRAC points ($S_\nu > 2 \times 10^4$ μJy) in our integration, as they deviate sharply from the flat, Euclidean trend expected at very bright fluxes in the right panel of Figure 2 owing to cosmic variance. After integrating and propagating through the statistical errors on each bin, we obtain an 8 μm CIB flux of 3.02 ± 0.09 nW m^{-2} sr^{-1}, slightly larger than estimates from 8 μm Spitzer surveys (2.6 nW m^{-2} sr^{-1}; Fazio et al. 2004).

Driver et al. (2016) estimated the CIB at 8 μm using Spitzer/IRAC data from Barmby et al. (2008), who surveyed 0.38 deg^2 in the Extended Groth Strip. Their uncertainty from cosmic variance ($\pm$0.08 mag) translates to approximately $\pm$0.035 mag for the 10 deg^2 area we have used to anchor our counts at bright levels (Ashby et al. 2009). They overstate the zero-point error; the absolute calibration of the IRAC data is accurate to $\sim$3%. The ultradeep JWST data basically remove uncertainties due to extrapolation to low fluxes. The net error in our value should therefore be $\sim$10%.

We calculate number counts at 21/24 μm in the same manner, by combining Spitzer/MIPS counts (Papovich et al. 2004) and our new MIRI SMILES counts. We remove the brightest MIRI 21 μm points ($S_\nu > 200$ μJy), which are most affected by cosmic variance. The 80% completeness limit for the Papovich et al. (2004) MIPS data lies at $S_\nu \sim 100$ μJy, so we do not include any fainter MIPS counts in our integration. The SMILES/MIRI and MIPS points agree very well (see Figure 3) near this remaining small region of overlap. We integrate from the faintest MIRI point (3.25 μJy) to the brightest MIPS point (4.76×10^4 μJy) and do not extrapolate; this integrated value is therefore a lower limit on the 21/24 μm CIB flux. Propagating through only the statistical errors on the counts, we obtain a flux of 2.85 ± 0.04 nW m^{-2} sr^{-1}. Since we have taken our bright 24 μm counts from the same source as Driver et al. (2016), their estimate of a cosmic variance error of $\pm$0.07 also applies to our result. Most other errors listed in Driver et al. (2016) should be reduced by use of the JWST data. As before, the zero-point error is significantly overstated; the absolute calibration of MIPS is accurate to $\sim$3% (Rieke et al. 2008). We conclude that the total error in our value is, as at 7.8 μm, $\sim$10%.

Béthermin et al. (2010) found a CIB flux of 2.29 ± 0.09 nW m^{-2} sr^{-1} from Spitzer 24 μm counts probing fluxes $>$35 μJy. However, when the counts were extrapolated at the faint end, they calculated an integrated 24 μm CIB flux of $2.86^{+0.19}_{-0.16}$ nW m^{-2} sr^{-1}, in excellent agreement with our value. Dole et al. (2006) also measured the 24 μm CIB by adding ;up the flux from all sources brighter than 60 μJy and using the counts of Papovich et al. (2004) to determine the contribution from fainter sources, finding an EBL value of 2.7 ± 0.26 nW m^{-2} sr^{-1}. Because Dole et al. (2006) do not quote any additional error from the extrapolation to very faint limits, this uncertainty is likely somewhat underestimated.

TeV gamma rays are attenuated as they traverse intergalactic space through pair production with the ambient ultraviolet, optical, and IR photons. SAMs of the history of galaxy formation and galaxy properties can be combined with TeV gamma-ray measurements to predict the spectrum of the EBL. Our values at both 7.8 and 24 μm are in mild tension with the fiducial EBL model based on TeV gamma-ray sources by Gilmore et al. (2012), which predicts values of 2.4 nW m^{-2} sr^{-1} at both wavelengths. As shown by Abeysekara et al. (2019), the highest weight values based on TeV gamma-ray observations tend to fall on or below the Gilmore fiducial, although the disagreement with our values is not huge. It should be kept in mind that the EBL estimates from source counts are strictly lower limits, since they exclude any diffuse emission and discriminate against extended sources. The discrepancy might therefore be larger than indicated here. These accurate determinations of the mid-IR EBL suggest that some tuning of the SAMs used to predict the EBL may be desirable.

5. Summary and Conclusions

We measure JWST/MIRI source counts from 5 to 25 μm using data from SMILES and JADES. We combine these unprecedentedly deep counts with existing, wider data from Spitzer and AKARI to produce counts spanning, in some bands, five or more orders of magnitude in flux. The uncertainties on our counts from cosmic variance and spurious sources are small.

When comparing our observed counts with predictions from a number of semianalytical models of galaxy formation, we find that the accuracy of the predicted counts is highly dependent on the templates used to construct model SEDs. In particular, models incorporating Spitzer/IRS spectroscopy of the PAH features from 6 to 12 μm more closely match our observed counts.

We integrate our deep JWST + wider-area Spitzer source counts at 8 and 24 μm to constrain the CIB at these wavelengths. Our results are consistent with those from shallower IR surveys that extrapolated their data at the faint end, but our deep data significantly reduce the associated uncertainty on the integrated EBL. Our results are strictly lower limits since our number counts are not sensitive to diffuse or extended emission. Nonetheless, we obtain larger EBL fluxes than predicted by fiducial EBL models based on TeV blazar data, suggesting that some tuning of the SAMs used for these predictions is needed.

Robust IR source counts spanning several orders of magnitude in flux can also be directly compared to predicted counts from models of galaxy formation. State-of-the-art models have large uncertainties at wavelengths longer than 8 μm. Our accurate counts should encourage generation of more robust models for comparison. Such modeling is also timely, since JWST's unique capabilities compared to any previous IR telescope will allow it to continue to provide critical constraints on models of galaxy formation and extragalactic light as larger areas of the sky are imaged to unprecedented depth.

Acknowledgments

M.S., S.A., G.R., J.L., and Y.Z. acknowledge support from the JWST Mid-Infrared Instrument (MIRI) grant 80NSSC18K0555 and the NIRCam science support contract NAS5-02105, both from NASA Goddard Space Flight Center to the University of Arizona. The JWST data presented in this paper were obtained from the Mikulski Archive for Space Telescopes (MAST) at the Space Telescope Science Institute. The observations can be accessed via doi:10.17909/zfxs-ye40. P.G.P.-G. acknowledges support from grant PID2022-139567NB-I00 funded by Spanish Ministerio de Ciencia e Innovación MCIN/AEI/10.13039/501100011033, FEDER *Una manera de hacer Europa*. A.J.B. acknowledges funding from the "FirstGalaxies" Advanced Grant from the European Research Council (ERC) under the European Union's Horizon 2020 research and innovation program (grant agreement No. 789056).

Facility: JWST (MIRI).

Software: Astropy (Astropy Collaboration et al. 2013, 2018), Matplotlib (Hunter 2007), NumPy (van der Walt et al. 2011), photutils (Bradley et al. 2022), WebbPSF (Perrin et al. 2014).

ORCID iDs

Meredith A. Stone https://orcid.org/0000-0002-9720-3255
Stacey Alberts https://orcid.org/0000-0002-8909-8782
George H. Rieke https://orcid.org/0000-0003-2303-6519
Andrew J. Bunker https://orcid.org/0000-0002-8651-9879
Jianwei Lyu (吕建伟) https://orcid.org/0000-0002-6221-1829
Pablo G. Pérez-González https://orcid.org/0000-0003-4528-5639
Irene Shivaei https://orcid.org/0000-0003-4702-7561
Yongda Zhu https://orcid.org/0000-0003-3307-7525

References

Abeysekara, A. U., Archer, A., Benbow, W., et al. 2019, ApJ, 885, 150
Alberts, S., Lyu, J., Shivaei, I., et al. 2024, arXiv:2405.15972
Alberts, S., Williams, C. C., Helton, J. M., et al. 2023, arXiv:2312.12207
Ashby, M. L. N., Stern, D., Brodwin, M., et al. 2009, ApJ, 701, 428
Ashby, M. L. N., Willner, S. P., Fazio, G. G., et al. 2015, ApJS, 218, 33
Astropy Collaboration, Price-Whelan, A. M., Sipőcz, B. M., et al. 2018, AJ, 156, 123
Astropy Collaboration, Robitaille, T. P., Tollerud, E. J., et al. 2013, A&A, 558, A33
Barmby, P., Huang, J. S., Ashby, M. L. N., et al. 2008, ApJS, 177, 431
Bernhard, E., Tadhunter, C., Mullaney, J. R., et al. 2021, MNRAS, 503, 2598
Béthermin, M., Dole, H., Beelen, A., & Aussel, H. 2010, A&A, 512, A78
Bisigello, L., Gruppioni, C., Feltre, A., et al. 2021, A&A, 651, A52
Bradley, L., Sipőcz, B., Robitaille, T., et al. 2022, astropy/photutils: v1.6.0, Zenodo, doi:10.5281/zenodo.7419741
Bushouse, H., Eisenhamer, J., Dencheva, N., et al. 2023, JWST Calibration Pipeline, v1.12.5, Zenodo, doi:10.5281/zenodo.10022973
Chary, R., Casertano, S., Dickinson, M. E., et al. 2004, ApJS, 154, 80
Clements, D. L., Bendo, G., Pearson, C., et al. 2011, MNRAS, 411, 373
Cowley, W. I., Baugh, C. M., Cole, S., Frenk, C. S., & Lacey, C. G. 2018, MNRAS, 474, 2352
Davidge, H., Serjeant, S., Pearson, C., et al. 2017, MNRAS, 472, 4259
Dole, H., Lagache, G., Puget, J. L., et al. 2006, A&A, 451, 417
Driver, S. P., Andrews, S. K., Davies, L. J., et al. 2016, ApJ, 827, 108
Driver, S. P., & Robotham, A. S. G. 2010, MNRAS, 407, 2131
Eisenstein, D. J., Willott, C., Alberts, S., et al. 2023, arXiv:2306.02465
Fazio, G. G., Ashby, M. L. N., Barmby, P., et al. 2004, ApJS, 154, 39
Gáspár, A., Rieke, G. H., Guillard, P., et al. 2021, PASP, 133, 014504
Giavalisco, M., Ferguson, H. C., Koekemoer, A. M., et al. 2004, ApJL, 600, L93
Gilmore, R. C., Somerville, R. S., Primack, J. R., & Domínguez, A. 2012, MNRAS, 422, 3189
Gispert, R., Lagache, G., & Puget, J. L. 2000, A&A, 360, 1
Granato, G. L., Lacey, C. G., Silva, L., et al. 2000, ApJ, 542, 710
Grogin, N. A., Kocevski, D. D., Faber, S. M., et al. 2011, ApJS, 197, 35
Hauser, M. G., Arendt, R. G., Kelsall, T., et al. 1998, ApJ, 508, 25
Hunter, J. D. 2007, CSE, 9, 90
Kirkpatrick, A., Yang, G., Bail, A. L., et al. 2023, ApJL, 959, L7
Lacy, M., Surace, J. A., Farrah, D., et al. 2021, MNRAS, 501, 892
Lagache, G., Puget, J.-L., & Dole, H. 2005, ARA&A, 43, 727
Lagos, C. d., Robotham, A. S. G., Trayford, J. W., et al. 2019, MNRAS, 489, 4196
Ling, C.-T., Kim, S. J., Wu, C. K. W., et al. 2022, MNRAS, 517, 853
Magdis, G. E., Daddi, E., Béthermin, M., et al. 2012, ApJ, 760, 6
Marleau, F. R., Fadda, D., Storrie-Lombardi, L. J., et al. 2004, ApJS, 154, 66
Moster, B. P., Somerville, R. S., Newman, J. A., & Rix, H.-W. 2011, ApJ, 731, 113
Murata, K., Pearson, C. P., Goto, T., et al. 2014, MNRAS, 444, 2346
Oliver, S. J., Goldschmidt, P., Franceschini, A., et al. 1997, MNRAS, 289, 471
Papovich, C., Dole, H., Egami, E., et al. 2004, ApJS, 154, 70
Papovich, C., Shipley, H. V., Mehrtens, N., et al. 2016, ApJS, 224, 28
Pearson, C. P., Oyabu, S., Wada, T., et al. 2010, A&A, 514, A8
Pearson, C. P., Serjeant, S., Oyabu, S., et al. 2014, MNRAS, 444, 846
Pérez-González, P. G., Barro, G., Rieke, G. H., et al. 2024, ApJ, 968, 4
Perrin, M. D., Sivaramakrishnan, A., Lajoie, C.-P., et al. 2014, Proc. SPIE, 9143, 91433X
Rieke, G. H., Blaylock, M., Decin, L., et al. 2008, AJ, 135, 2245
Rieke, M. J., Robertson, B., Tacchella, S., et al. 2023, ApJS, 269, 16
Robertson, B. E. 2010, ApJL, 716, L229
Rocca-Volmerange, B., de Lapparent, V., Seymour, N., & Fioc, M. 2007, A&A, 475, 801
Rowan-Robinson, M. 2001, NewAR, 45, 631
Rowan-Robinson, M. 2009, MNRAS, 394, 117
Rowan-Robinson, M. 2024, MNRAS, 527, 10254
Rowan-Robinson, M., Babbedge, T., Surace, J., et al. 2005, AJ, 129, 1183
Rowan-Robinson, M., Lari, C., Perez-Fournon, I., et al. 2004, MNRAS, 351, 1290
Schreiber, C., Elbaz, D., Pannella, M., et al. 2018, A&A, 609, A30
Silva, L., Granato, G. L., Bressan, A., & Danese, L. 1998, ApJ, 509, 103
Spoon, H. W. W., Moorwood, A. F. M., Lutz, D., et al. 2004, A&A, 414, 873
Teplitz, H. I., Chary, R., Elbaz, D., et al. 2011, AJ, 141, 1
Treister, E., Urry, C. M., Van Duyne, J., et al. 2006, ApJ, 640, 603
Trenti, M., & Stiavelli, M. 2008, ApJ, 676, 767
van der Walt, S., Colbert, S. C., & Varoquaux, G. 2011, CSE, 13, 22
Viero, M. P., Moncelsi, L., Quadri, R. F., et al. 2013, ApJ, 779, 32
Whitaker, K. E., Labbé, I., van Dokkum, P. G., et al. 2011, ApJ, 735, 86
Wu, C. K. W., Ling, C.-T., Goto, T., et al. 2023, MNRAS, 523, 5187
Yang, G., Papovich, C., Bagley, M. B., et al. 2023, ApJL, 956, L12